

Supplementary information

**High-resolution non-line-of-sight imaging
employing active focusing**

In the format provided by the
authors and unedited

High-resolution non-line-of-sight imaging employing active focusing: Supplementary Notes

Ruizhi Cao¹, Frederic de Goumoens¹, Baptiste Blochet¹, Jian Xu¹, and Changhui Yang^{1,2}

¹Department of Electrical Engineering, California Institute of Technology, Pasadena, CA, USA

²chyang@caltech.edu

1 Optimization pipeline

To sync the digital micro-mirror device (DMD) and acquire signal coming from the photomultiplier tube (PMT), we chose to acquire the DMD output trigger and the signal from the PMT simultaneously. An example of the pipeline for our second step to find the optimal phase mask for each of the sub-apertures is shown in Fig. S1, where 9 sub-apertures were chosen for illustration.

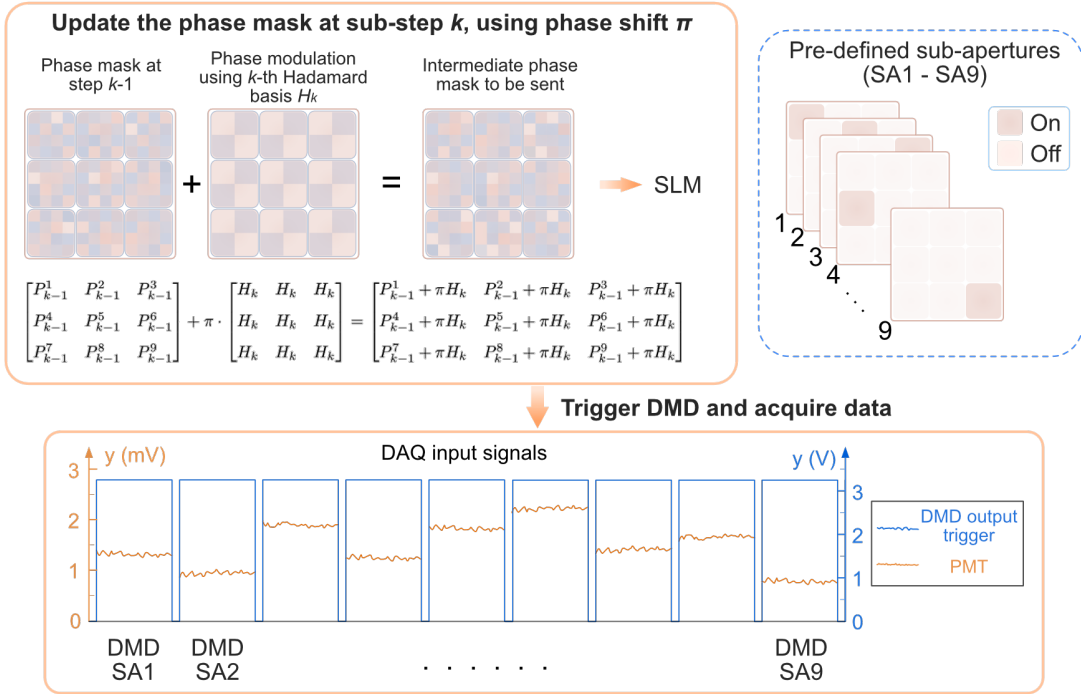


Figure S1: Pipeline for optimizing each of the sub-apertures. In this figure, 9 sub-apertures are used for illustration. SLM is used in combination with a DMD for a higher optimization speed. DMD is applied to select which sub-aperture to use in the optimization. At sub-step k , the same phase modulation is added to all the optimized phase masks at step $k - 1$. The newly generated phase mask is sent to SLM for updating. After SLM finishes updating, pre-defined sub-apertures are displayed sequentially by using the DMD. A small period of dark time is introduced to the DMD for discriminating signals from different sub-apertures. Signals within one of the blue window are averaged and the mean value is used in updating the phase mask. After finishing 4-step phase shift, the phase masks get updated and are used in step $k + 1$. DAQ, data-acquisition device, P_k^i denotes the phase mask at sub-step k for sub-aperture i (P_k^i is a N -by- N matrix), and H_k denotes the k -th Hadamard basis (also a N -by- N matrix).

If we want to optimize all the sub-apertures, one way is to simply perform the iterative algorithm for all sub-apertures sequentially. In this case, if we have N^2 independent modes in each sub-aperture and in total Q sub-apertures, we need to update the SLM $4N^2 \times Q$ times using 4-phase shifting method (Hadamard basis based algorithm) [1–5]. This is inefficient as, in each sub-step k , only a small part of the SLM gets refreshed, leaving a great number of pixels unchanged. As optimizing one sub-aperture is independent of optimizing another, we use the same Hadamard pattern to modulate all the sub-apertures at each sub-step k . Thus, we can update all the phase masks by sending only one image to the SLM. We note that we still want to get the feedback signal with contribution from only one sub-aperture. Thus, we still need to block light from other sub-apertures when doing the measurement. This is done by using a much faster DMD (with a refresh rate of 9500 Hz for displaying binary patterns), which is simply used to select which sub-aperture to use during the optimizing process. In this case, patterns sent to SLM need only to be updated $4N^2$ times. This strategy is used in our experiment.

We first load the pre-defined sub-apertures (SA1 to SA9) into the buffer of DMD, the exposure time for all the patterns is defined at the beginning. A short period of dark time is also defined in order to discriminate signals when using different sub-apertures. All sub-apertures are initiated with zeros at the beginning. At sub-step k , the positive entries of the k -th Hadamard pattern are phase modulated using $0, \pi/2, \pi,$ and $3\pi/2$ [1–5].

Figure S1 shows the modulation step for phase modulation π . The intermediate phase mask is sent to SLM and signals from all the sub-apertures are acquired sequentially. After the signals for all the phase modulation are acquired, the phase mask is then updated. This step is repeated until the number of iterations reaches a predefined number.

If we write the feedback signal for SA i under the four different modulations as $S_1^i, S_2^i, S_3^i,$ and S_4^i respectively, the best phase at sub-step k is

$$\varphi_{\text{best}}^{i,k} = \arg [(S_1^i - S_3^i) + j \cdot (S_2^i - S_4^i)], \quad (\text{S1})$$

where $\arg(\cdot)$ takes the argument of a complex number, j is the unit imaginary number. Then, the phase mask of the i -th sub-aperture is updated in the following way:

$$P_k^i = P_{k-1}^i + \varphi_{\text{best}}^{i,k} H_k. \quad (\text{S2})$$

After the optimal phase solution for each of the sub-apertures has been obtained, we will start using pairs to optimize the relative phase offset among all the sub-apertures.

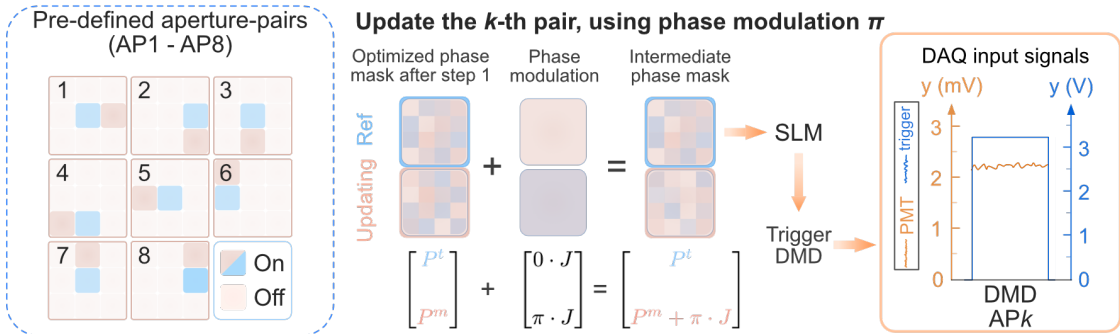


Figure S2: Using pairs to find the phase offset. The blue color in the pre-defined sub-apertures denotes the reference in use, and the other highlighted sub-aperture is the one being updated. To update the k -th pair, phase offsets of $0, \pi/2, \pi,$ and $3\pi/2$ are added to the sub-aperture being updated. For each of the phase offset, the intermediate phase mask is sent to SLM. After SLM finishes refreshing, DMD is triggered to display the k -th aperture-pair, AP k . The best phase offset is then calculated and added to the sub-aperture being updated using 4-step phase shifting method. P^t is the reference for the k -th pair (AP k), P^m the sub-aperture to be updated, and J an matrix with all 1's whose dimension is the same as P^t & P^m .

For tuning the phase offset among all the sub-apertures, we chose to update the phase offset along a spiral line, as shown in Step 3 of Fig. 2 in the main paper. Here, we showed a detailed example of the pairs when using 9 sub-apertures in total (Fig. S2). These pre-defined pairs are preloaded into the DMD for higher

refresh rate. To update the k -th pair, the sub-aperture highlighted in blue, P^t , is chosen as the reference and keeps untouched in this step. Phase offset of $0, \pi/2, \pi$, and $3\pi/2$ is added sequentially to the one to be updated (P^m), and generates an intermediate phase mask. This intermediate phase mask is uploaded to the SLM and feedback signals is then acquired by triggering the DMD to display the k -th aperture-pair (APk). Once the best phase offset that maximizes the feedback signal is obtained, this offset is directly added on P^m , which may then be used as a reference in the following steps.

If we write the feedback signals for updating the m -th sub-aperture (P^m) as $\hat{S}_1^m, \hat{S}_2^m, \hat{S}_3^m$, and \hat{S}_4^m respectively, the optimal phase offset for P^m is:

$$\Phi_{\text{best}}^m = \arg \left[(\hat{S}_1^m - \hat{S}_3^m) + j \cdot (\hat{S}_2^m - \hat{S}_4^m) \right]. \quad (\text{S3})$$

And the phase mask of the m -th sub-aperture is updated:

$$P_{\text{updated}}^m = P^m + \Phi_{\text{best}}^m. \quad (\text{S4})$$

If the phase offsets have been obtained for all the sub-apertures, a sharp focus is generated when we open up all the sub-apertures and apply the optimized phase mask. This focus is then raster-scanned to get an image of the target.

2 Derivation of UNCOVER

In the following section, we provide a framework for analyzing UNCOVER. We will start from the simplest example where we want to align two phasors to maximize the feedback signal. Then, we will extend the approach used in this toy example to find the solution of the maximizing problem for one of the sub-apertures. The intuition comes from the idea that when the size of the sub-aperture is confined in a way such that the speckle size (which is approximately equal to the focus size after optimization) is larger than the object, the object can be treated as a fixed point (i.e. the location of the point is independent of the selection of sub-aperture).

To synthesize all the sub-apertures, we want the foci generated by the sub-apertures to interfere constructively at the same point (thus enable us to generate a sharp focus). We will see that, with constraint on the size of the sub-aperture pairs applied in the optimization step, the object acts as a fixed point throughout the optimization. We will show that a final focus is formed on the center of mass of the object function, which will be defined later on.

2.1 The maximizing problem for one of the sub-apertures

Before we dive into the details, we will first state the assumption of UNCOVER and derive the constraints on the object such that 3D objects can be approximated as 2D objects. The derivations from Proposition 2.1.1 to Eq. S21 prove that 3D objects can be treated as 2D objects with constraint on the axial extent of the 3D objects. After we have proven that 2D approximation is feasible, we will conduct our analysis and derive the result based on 2D objects.

Assumption 2.1.1 *Assume the distance between the wall and the object is large, so that light emitting from each mode of one sub-aperture can be approximated as a plane wave over the (volume of) the hidden objects.*

Using the above assumption, the speckle incidents on the object caused by light interfering from one of sub-apertures can be written as

$$\sum_n A_n(\mathbf{k}_n) e^{i(\mathbf{k}_n \mathbf{r} + \phi_n)}, \quad (\text{S5})$$

where \mathbf{k}_n is the wave vector for input mode n , A_n the amplitude of input mode n , \mathbf{r} the spatial location and ϕ_n the phase of that mode.

Let us first consider a 3D object function $O(\mathbf{r}) = O(x, y, z)$, the signal received by the detector, E , is given by

$$E = \int_O I(\mathbf{r}) \cdot O(\mathbf{r}) d\mathbf{r} = \iiint I(x, y, z) \cdot O(x, y, z) dx dy dz. \quad (\text{S6})$$

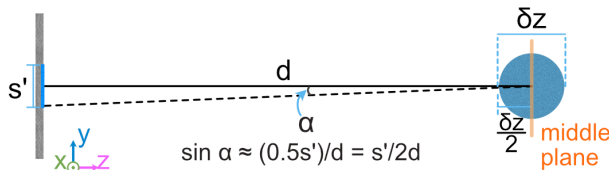


Figure S3: Variables in proposition 2.1.1. The angles shown here are for illustration and do not correspond to the angles in our experiments.

Proposition 2.1.1 *Under assumption 2.1.1, let's further assume that the size of the sub-aperture, denoted by s' , is much less than the distance d between the wall and the object. The illumination pattern is approximately independent of z , given the axial extent δz satisfies the following constraint:*

$$\delta z \leq \min \left\{ 0.2d, \frac{1}{10} DOF_{sub-aperture} \right\}, \quad (\text{S7})$$

where $DOF_{sub-aperture}$ is the depth of field of the sub-aperture, and is defined using the formula of DOF in microscopy: $DOF_{sub-aperture} = \frac{\lambda}{NA^2}$.

Proof:

Based on the assumption in Proposition 2.1.1, we have (α is the one-half angular aperture):

$$\text{NA}' := \text{NA}_{\text{sub-aperture}} = n_{\text{air}} \cdot \sin \alpha = \sin \alpha \approx \frac{s'}{2d} \ll 1, \quad (\text{S8})$$

and

$$\delta z \leq \frac{1}{10} \text{DOF}_{\text{sub-aperture}} = \frac{1}{10} \frac{\lambda}{\text{NA}'^2} = \frac{2\lambda d^2}{5s'^2}. \quad (\text{S9})$$

Note that Proposition 2.1.1 is based on Assumption 2.1.1, so we want the direction of \mathbf{k}_n to remain the same over δz .

Let us first assume $\frac{\delta z}{2} \ll d$. To investigate what the constraint is, we will write the k -vector of mode n at axial position z' as $\mathbf{k}_n(z')$ for now (z' is some arbitrary value here). The direction change of $\mathbf{k}_n(z')$ can be characterized by the change in the polar angle $\alpha_n(z')$ of $\mathbf{k}_n(z')$, as the azimuthal angle in spherical coordinates is independent of z in Cartesian coordinates. If the tolerance of the absolute rate of change in $\alpha_n(z')$ is set to 0.1 when $z' \in [d - \frac{\delta z}{2}, d + \frac{\delta z}{2}]$, we require (we have $\delta z \ll 2d$):

$$\begin{aligned} \left| \alpha_n(d) - \alpha_n(d \pm \frac{\delta z}{2}) \right| &\approx \left| \frac{s}{2d} - \frac{s}{2d \pm \delta z} \right| = \left| \frac{s}{2d} - \frac{s}{2d} \frac{1}{(1 \pm \frac{\delta z}{2d})} \right| \approx \frac{s}{2d} \left| 1 - (1 \mp \frac{\delta z}{2d}) \right| \leq 0.1 \alpha_n(d) \approx \frac{s}{20d} \\ &\Rightarrow \delta z \leq 0.2d. \end{aligned} \quad (\text{S10})$$

To summarize, we get

$$\delta z \leq \min \left\{ 0.2d, \frac{2\lambda d^2}{5s'^2} \right\}. \quad (\text{S11})$$

If the above is satisfied, the Assumption 2.1.1 holds, and \mathbf{k}_n is independent of z . Thus, in our following derivation, \mathbf{k}_n can be regarded as a constant vector. The E-field E_f of the illumination pattern at $(x, y, d + \Delta z)$ is:

$$E_f(x, y, d + \Delta z) = E_f(\mathbf{r} + \Delta \mathbf{z}) = \sum_n A_n(\mathbf{k}_n) e^{i(\mathbf{k}_n \cdot (\mathbf{r} + \Delta \mathbf{z}) + \phi_n)} = \sum_n A_n(\mathbf{k}_n) e^{i(\mathbf{k}_n \cdot \mathbf{r} + \phi_n)} e^{ik_{n,z} \Delta z}. \quad (\text{S12})$$

Let us focus on the factor $e^{ik_{n,z} \Delta z}$. For the z -component of \mathbf{k}_n , we have (α_n is the polar angle of \mathbf{k}_n in spherical coordinates):

$$k_{n,z} = |\mathbf{k}_n| \cos(\alpha_n) = \frac{2\pi}{\lambda} \sqrt{1 - \sin^2(\alpha_n)} \approx \frac{2\pi}{\lambda} - \frac{\pi}{\lambda} \sin^2(\alpha_n), \quad (\text{S13})$$

where $\alpha_n \in [-\alpha, \alpha]$, as α is the one-half angular aperture. Thus, we have

$$|k_{n,z} - k_{m,z}| \leq \max_n k_{n,z} - \min_m k_{m,z} = \frac{2\pi}{\lambda} - \left(\frac{2\pi}{\lambda} - \frac{\pi}{\lambda} \sin^2(\alpha) \right) = \frac{\pi}{\lambda} \sin^2(\alpha). \quad (\text{S14})$$

The absolute phase retardation between input mode n and input mode m over Δz is bounded above by:

$$|k_{n,z} \Delta z - k_{m,z} \Delta z| = |k_{n,z} - k_{m,z}| \Delta z \leq \frac{\pi}{\lambda} \sin^2(\alpha) \Delta z. \quad (\text{S15})$$

Plug in Eq. S11 and use the fact that $\Delta z \in [-\frac{\delta z}{2}, \frac{\delta z}{2}]$,

$$|k_{n,z} - k_{m,z}| \Delta z \leq \frac{\pi}{\lambda} \sin^2(\alpha) \Delta z \leq \frac{\pi}{\lambda} \sin^2(\alpha) \frac{\delta z}{2} \leq \frac{\pi}{\lambda} \sin^2(\alpha) \cdot \frac{1}{20} \frac{\lambda}{\text{NA}'^2} = \frac{\pi}{20}. \quad (\text{S16})$$

That is, the maximum path length difference over the axial extent of the 3D object function is $\frac{\lambda}{40}$. (Note that this is a strict criterion and can be eased.) Such a small phase retardation between different input modes can be ignored:

$$e^{ik_{n,z} \Delta z} \approx e^{ik_{m,z} \Delta z} = e^{i\theta_0}, \quad \forall n, m. \quad (\text{S17})$$

Then, we have

$$E_f(x, y, d + \Delta z) = \sum_n A_n(\mathbf{k}_n) e^{i(\mathbf{k}_n \mathbf{r} + \phi_n)} e^{ik_{n,z} \Delta z} \approx e^{i\theta_0} \sum_n A_n(\mathbf{k}_n) e^{i(\mathbf{k}_n \mathbf{r} + \phi_n)} = e^{i\theta_0} E_f(x, y, d). \quad (\text{S18})$$

The intensity $I(x, y, z + \Delta z)$ is given by:

$$I(x, y, d + \Delta z) = E_f(x, y, d + \Delta z) \cdot E_f^*(x, y, d + \Delta z) = E_f(x, y, d) \cdot E_f^*(x, y, d) = I(x, y, d). \quad (\text{S19})$$

So, within the range $z \in [d - \frac{\delta z}{2}, d + \frac{\delta z}{2}]$, the illumination pattern is independent of z and can be written as a function of (x, y) only:

$$I(\mathbf{r}) = I(x, y, z) = I(x, y). \quad (\text{S20})$$

The signal E can be simplified:

$$\begin{aligned} E &= \iiint I(x, y, z) \cdot O(x, y, z) dx dy dz = \iint dx dy \int_{d - \frac{\delta z}{2}}^{d - \frac{\delta z}{2}} I(x, y) \cdot O(x, y, z) dz \\ &= \iint dx dy I(x, y) \cdot \int_{d - \frac{\delta z}{2}}^{d - \frac{\delta z}{2}} O(x, y, z) dz = \iint I(x, y) \cdot O'(x, y) dx dy, \end{aligned} \quad (\text{S21})$$

where $O'(x, y) := \int O(x, y, z) dz$ is the projection of $O(x, y, z)$ onto the xy -plane.

Thus, we prove Proposition 2.1.1, which means a 3D object is equivalent to a 2D object when the assumptions in the proposition hold. Note that more sophisticated maps can be used for the 3D to 2D transformation, such as using cones to map the 3D objective function to a particular xy -plane. More works can be done in this direction.

In the following derivation, we will assume a 2D object function is used, otherwise it can be projected onto a 2D plane by using Proposition 2.1.1. And we are interested only in the 2D coordinates that involve (x, y) .

In iterative wavefront shaping, we only modulate the phase of each input mode, and the output field with the phase modulation applied can be written as:

$$\sum_n A_n(\mathbf{k}_n) e^{i(\mathbf{k}_n \mathbf{r} + \phi_n + p_n)}, \quad (\text{S22})$$

where p_n is the phase modulation we applied, $\mathbf{k}_n = [k_x, k_y]^T$ and $\mathbf{r} = [x, y]^T$. We define the maximum length l_{\max} of an object A as:

$$l_{\max} = \max\{|\mathbf{r}_1 - \mathbf{r}_2| : A(\mathbf{r}_1) \neq 0, A(\mathbf{r}_2) \neq 0\}, \quad (\text{S23})$$

where $|\cdot|$ is Euclidean norm.

Assumption 2.1.2 Assume the maximum length of the object O , l_{\max} , satisfies $\forall n, m : |\mathbf{k}_n - \mathbf{k}_m| l_{\max} < \pi$ (The smallest period of the fringes is larger than l_{\max}).

The total energy detected $E(\mathbf{p})$ is given by:

$$\begin{aligned} E(\mathbf{p}) &= \int_O O(\mathbf{r}) I(\mathbf{r}) d\mathbf{r} = \int_O O(\mathbf{r}) \left(\sum_n A_n(\mathbf{k}_n) e^{i(\mathbf{k}_n \mathbf{r} + \phi_n + p_n)} \right) \cdot \left(\sum_m A_m(\mathbf{k}_m) e^{-i(\mathbf{k}_m \mathbf{r} + \phi_m + p_m)} \right) d\mathbf{r} \\ &= \int_O O(\mathbf{r}) \left[\sum_n A_n^2(\mathbf{k}_n) + 2 \sum_{n < m} \text{Re} \left(A_n(\mathbf{k}_n) A_m(\mathbf{k}_m) e^{i(\Delta \mathbf{k}_{nm} \mathbf{r} + \Delta \phi_{nm} + \phi_n - \phi_m + p_n - p_m)} \right) \right] d\mathbf{r} \\ &\propto c + \int_O O(\mathbf{r}) \sum_{n < m} \text{Re} \left(A_n(\mathbf{k}_n) A_m(\mathbf{k}_m) e^{i(\Delta \mathbf{k}_{nm} \mathbf{r} + \Delta \phi_{nm} + \Delta p_{nm})} \right) d\mathbf{r}, \end{aligned} \quad (\text{S24})$$

where $\mathbf{p} = [p_1, p_2, \dots, p_n]^T$, $\Delta \mathbf{k}_{nm} = \mathbf{k}_n - \mathbf{k}_m$, $\Delta \phi_{nm} = \phi_n - \phi_m$, $\Delta p_{nm} = p_n - p_m$, $c \in \mathbb{R}$ some constant independent of \mathbf{p} , and $O(\mathbf{r})$ is the fraction of light being diffused by the object at \mathbf{r} (the object function).

Question What is the best \mathbf{p} that maximizes the integral?

In the following section, we will see that maximizing the total energy detected is equivalent to maximizing the intensity over a certain point, which is the same as using a point guidestar.

2.2 Solution

To find out the solution for Eq. S24, we start by considering the interference of two phasors $A_n(\mathbf{k}_n)e^{i(\mathbf{k}_n\mathbf{r}+\phi_n+p_n)}$ and $A_m(\mathbf{k}_m)e^{i(\mathbf{k}_m\mathbf{r}+\phi_m+p_m)}$. The interference of the two point sources results in a sinusoidal pattern on the object. By studying this simple case, we will know at what point the integral is maximized. If, by some happenstance, the optimal point is the same for any two phasors we choose, the global maximum will also be achieved at that point. And we will shortly see that this is indeed the case. We will first define the center of mass of the object's reflection function $O(\mathbf{r})$: (we will see, after all these derivations, that this is the point that all phasors are aligned.)

Definition 2.2.1 Define the center of mass C_m of an object O as:

$$C_m = \frac{\int_O O(\mathbf{r})\mathbf{r}d\mathbf{r}}{\int_O O(\mathbf{r})d\mathbf{r}}. \quad (\text{S25})$$

Without loss of generality, let us focus on $\Delta\mathbf{k}_{nm}$, and set up a Cartesian coordinate such that the direction of the positive x-axis is the same as the direction of $\Delta\mathbf{k}_{nm}$ ($k := k_x = |\Delta\mathbf{k}_{nm}|$), and let the origin be C_m . Given \mathbf{k}_n and \mathbf{k}_m , we have:

$$\begin{aligned} & \int_O O(\mathbf{r})\text{Re}\left(A_n(\mathbf{k}_n)A_m(\mathbf{k}_m)e^{i(\Delta\mathbf{k}_{nm}\mathbf{r}+\Delta\phi_{nm}+\Delta p_{nm})}\right)d\mathbf{r} \\ &= A_n(\mathbf{k}_n)A_m(\mathbf{k}_m)\int dx\int O(x,y)\text{Re}\left(e^{i(kx+\Delta\phi_{nm}+\Delta p_{nm})}\right)dy \\ &= a_{nm}\int \text{Re}\left(e^{i(kx+\Delta\phi_{nm}+\Delta p_{nm})}\right)\left(\int O(x,y)dy\right)dx \\ &= a_{nm}\int f(x)\cos(kx+\Delta\phi_{nm}+\Delta p_{nm})dx \\ &= a_{nm}\int_{-\frac{\pi}{k}}^{\frac{\pi}{k}} f(x)\cos(kx+\Delta\phi_{nm}+\Delta p_{nm}), \end{aligned} \quad (\text{S26})$$

where $f(x) = \int O(x,y)dy \geq 0$, $a_{nm} = A_n(\mathbf{k}_n)A_m(\mathbf{k}_m) > 0$ (For the last step of Eq. S26, note that we have $\forall n, m : |\mathbf{k}_n - \mathbf{k}_m| < \pi$ based on Assumption 2.1.2). Also, as we define the origin to be C_m , we have:

$$\int xf(x)dx = 0. \quad (\text{S27})$$

Let us study this function:

$$F(k, \alpha) = \int_{-\frac{\pi}{k}}^{\frac{\pi}{k}} f(x)\cos(kx+\alpha)dx. \quad (\text{S28})$$

Lemma 2.2.1 $\forall f(x), \exists \alpha : \int_{-\frac{\pi}{k}}^{\frac{\pi}{k}} f(x)\cos(kx+\alpha)dx \geq 0$

Proof Assume $\forall f(x), \alpha : \int_{-\frac{\pi}{k}}^{\frac{\pi}{k}} f(x)\cos(kx+\alpha)dx < 0$. Let $\alpha' = \alpha + \pi$ we have:

$$\int_{-\frac{\pi}{k}}^{\frac{\pi}{k}} f(x)\cos(kx+\alpha')dx = \int_{-\frac{\pi}{k}}^{\frac{\pi}{k}} f(x)\cos(kx+\alpha+\pi)dx = -\int_{-\frac{\pi}{k}}^{\frac{\pi}{k}} f(x)\cos(kx+\alpha)dx > 0.$$

This leads to a contradiction. Thus, we have that for all $f(x)$, there exists α such that

$$\int_{-\frac{\pi}{k}}^{\frac{\pi}{k}} f(x)\cos(kx+\alpha)dx \geq 0. \quad (\text{S29})$$

As we want to maximize $F(k, \alpha)$, let us confine the range of α such that $\forall \alpha \in S : F(k, \alpha) \geq 0$, where S is the constraint set:

$$S := \{\forall \alpha \in S : F(k, \alpha) = \int_{-\frac{\pi}{k}}^{\frac{\pi}{k}} f(x)\cos(kx+\alpha)dx \geq 0\}. \quad (\text{S30})$$

Assume F and its first and second order of partial derivatives are all continuous (it satisfies Leibniz's rule), let us find the partial derivative of $F(k, \alpha)$ with respect to α :

$$\frac{\partial F(k, \alpha)}{\partial \alpha} = \int_{-\frac{\pi}{k}}^{\frac{\pi}{k}} f(x) \frac{\partial \cos(kx + \alpha)}{\partial \alpha} dx = - \int_{-\frac{\pi}{k}}^{\frac{\pi}{k}} f(x) \sin(kx + \alpha) dx; \quad \alpha \in S \quad (\text{S31})$$

$$\frac{\partial^2 F(k, \alpha)}{\partial \alpha^2} = - \int_{-\frac{\pi}{k}}^{\frac{\pi}{k}} f(x) \frac{\partial \sin(kx + \alpha)}{\partial \alpha} dx = - \int_{-\frac{\pi}{k}}^{\frac{\pi}{k}} f(x) \cos(kx + \alpha) dx \leq 0; \quad \alpha \in S \quad (\text{S32})$$

The second order partial derivative is non-positive. Thus, to maximize $F(k, \alpha)$, we simply need to solve for this equation:

$$\int_{-\frac{\pi}{k}}^{\frac{\pi}{k}} f(x) \sin(kx + \alpha) dx = 0. \quad (\text{S33})$$

Note that if we want to have a well defined focus (all the phasors are optimized such that they are all in phase at a certain point), we want Eq. S33 holds for all k at a certain $x_0 = \frac{\alpha}{k}$.

Let's look at an extreme case: $k \rightarrow 0$. In this case, we have

$$\lim_{k \rightarrow 0} \int_{-\frac{\pi}{k}}^{\frac{\pi}{k}} f(x) \sin(kx + \alpha) dx = \int_{-\frac{\pi}{k}}^{\frac{\pi}{k}} f(x) \sin(\alpha) dx = 0. \quad (\text{S34})$$

We know that $f(x) = \int O(x, y) dy \geq 0$ (light energy returned to detector cannot be negative), so to solve Eq. S34 we get

$$\sin(\alpha) = 0 \Rightarrow \alpha = 0. \quad (\text{S35})$$

In the above equation, we limit $\alpha \in (-\pi, \pi] \cap S$. Thus, another possible solution $\alpha = \pi$ is dropped based on the fact that $\lim_{k \rightarrow 0} \int_{-\frac{\pi}{k}}^{\frac{\pi}{k}} f(x) \cos(kx + \alpha) dx = \int_{-\frac{\pi}{k}}^{\frac{\pi}{k}} f(x) \cos(\pi) dx = - \int_{-\frac{\pi}{k}}^{\frac{\pi}{k}} f(x) dx < 0$. Hence it does not belong to the constraint set $\alpha = \pi \notin S$.

As Eqs. S33 and S35 need to hold for all k , we need the following equation holds

$$\int_{-\frac{\pi}{k}}^{\frac{\pi}{k}} f(x) \sin(kx) dx = 0. \quad (\text{S36})$$

Condition 2.2.1 *The object $O(x, y)$ has point symmetry with respect to its center of mass, which means $O(x, y) = O(-x, -y)$. And l_{max} is less or equal to $\frac{1}{\max|\Delta \mathbf{k}|}$.*

Using the above condition, we have

$$f(-x) = \int O(-x, y) dy = \int O(x, y) dy = f(x). \quad (\text{S37})$$

We can easily verify that Eq. S36 holds in this case.

For a more general case in which the object is of arbitrary shape, let us use Taylor expansion to rewrite the left hand side of Eq. S36. This gives

$$\int_{-\frac{\pi}{k}}^{\frac{\pi}{k}} f(x) \sin(kx) dx = \int_{-\frac{\pi}{k}}^{\frac{\pi}{k}} f(x) \left(kx - \frac{(kx)^3}{3!} + \frac{(kx)^5}{5!} - \dots \right) dx. \quad (\text{S38})$$

Condition 2.2.2 *The maximum length l_{max} of the object O is much smaller than $\frac{1}{\max|\Delta \mathbf{k}|}$*

Using condition 2.2.2, Eq. S38 becomes

$$\int_{-\frac{\pi}{k}}^{\frac{\pi}{k}} f(x) \sin(kx) dx \approx k \int_{-\frac{\pi}{k}}^{\frac{\pi}{k}} x f(x) dx = 0. \quad (\text{S39})$$

If we want the error of the approximation $\sin(kx) \approx kx$ smaller than 10^{-3} , we need $\frac{(\max|\Delta \mathbf{k}| l_{max})^3}{3!} < 10^{-3}$. That is, we want $l_{max} < \frac{0.18}{\max|\Delta \mathbf{k}|}$.

2.3 Conclusion and connection to UNCOVER

If Eq. S36 holds, let's go back to the last term of Eq. S24:

$$\begin{aligned} & \int_O O(\mathbf{r}) \sum_{n < m} \operatorname{Re} \left(A_n(\mathbf{k}_n) A_m(\mathbf{k}_m) e^{i(\Delta \mathbf{k}_{nm} \mathbf{r} + \Delta \phi_{nm} + \Delta p_{nm})} \right) d\mathbf{r} \\ & \leq \int_O O(\mathbf{r}) \sum_{n < m} \operatorname{Re} \left(A_n(\mathbf{k}_n) A_m(\mathbf{k}_m) e^{i(\Delta \mathbf{k}_{nm} \mathbf{r})} \right) d\mathbf{r}. \end{aligned} \quad (\text{S40})$$

Thus, we obtain

$$\operatorname{argmax}_{\mathbf{p}} E(\mathbf{p}) = -\phi + p_0, \quad (\text{S41})$$

where p_0 is a constant and $\phi = [\phi_1, \phi_2, \dots, \phi_n]^T$.

The **sufficient** condition that guarantees we will have a well defined focus is given by **Condition 2.2.1** or **Condition 2.2.2** under **Assumption 2.1.1** and **Assumption 2.1.2**. This indicates that, under certain conditions, if the speckle size generated by one sub-aperture is larger than the object, the object can be treated as a point.

These two conditions basically mean that if the object is centrosymmetric or the maximum length of the object is smaller than the smallest period produced by the sub-aperture, then the algorithm described in the beginning would give us a focus. And the center of the focus coincides with the center of mass (C_m , Definition 2.2.1) of the object function. The intuition for this is that when the period is larger than the object (it won't be able to resolve the object), the hidden object can be treated as a point.

Coming back to UNCOVER, one wants a tight focus that can be raster scanned over the object itself. To realize a tight focus, we want all the phasors for the full aperture are aligned at a certain point.

In sections 2.1 and 2.2, we derived that if size of the aperture is carefully selected, the hidden object can be treated as a point source at C_m . That is, if the size the illuminated area (aperture) at any instant in the optimization algorithm satisfy a certain constraint (e.g. the focus size of the optimized aperture is larger than the object), a focus can be formed at C_m , the position of the equivalent point guidestar.

To optimize the phase masks in Step 2, the sub-apertures are designed such that they are small enough to satisfy the aforementioned constraints (Note that this is not the ultimate requirement on the size of sub-apertures, we will discuss a further constraint in the following two paragraphs). With the constraints being satisfied, only a single focus with its center at C_m is obtained for each sub-aperture in Step 2.

The next question is how to synthesize those sub-apertures so that they produce one tight focus on the object. If a tight focus is desired, we want the hidden object to act like a point guidestar when adjusting the phase offset among the sub-apertures. That is, we want the constraints on the size of the aperture to be satisfied at any instance throughout Step 3 of the optimization algorithm.

The constraint on the size of aperture that is simultaneously used in Step 3 is satisfied by using pairs. We designed the sub-apertures such that when opening any two adjacent sub-apertures, the speckle size is still larger than the object size (which meets the constraints stated above). Following the result we have in section 2.2, the hidden object serves as a point. Let us focus on what happens to this point. If we write \tilde{A}_i and $\tilde{\gamma}_i$ as the amplitude and the phase of the focus of i -th optimized sub-aperture, respectively. Maximizing the signal scattered by the hidden object over the phase offset $\tilde{\omega}$ is equivalent to

$$\operatorname{argmax}_{\tilde{\omega}} |\tilde{A}_t e^{i\tilde{\gamma}_t} + \tilde{A}_m e^{i\tilde{\gamma}_m + i\tilde{\omega}}|^2, \quad (\text{S42})$$

where t denotes the reference sub-aperture and m denotes the sub-aperture to be updated in the k -th pair. Note that this is true only when the hidden target is equivalent to a point guidestar.

The optimal solution is given by

$$\tilde{\gamma}_m + \tilde{\omega}_{\text{best}} = \tilde{\gamma}_t. \quad (\text{S43})$$

Thus, using Eq. S4, the phase of the updated m -th sub-aperture is

$$\tilde{\gamma}_m^{\text{updated}} = \tilde{\gamma}_m + \tilde{\omega}_{\text{best}} = \tilde{\gamma}_t. \quad (\text{S44})$$

That is, all the sub-aperture in the reference library share the same phase at C_m . Thus, when the optimization is performed over all sub-aperture pairs, light from all sub-aperture interferes constructively at C_m . Thus, after Step 3 is finished, a tight focus is generated at C_m when the full-aperture is used (Note that the phase masks are applied directly and no optimization is needed).

2.4 Discussion on the algorithm

To use UNCOVER, we want the sub-aperture pairs to satisfy a certain constraint, which is related to the size of the hidden objects. Thus, an estimate of the hidden objects' size is needed. However, it's worthwhile to point out that, such prior knowledge is unnecessary if UNCOVER is performed multiple times with different sub-aperture sizes in each trial. In Fig. S6, it is shown that UNCOVER scanned images converge when UNCOVER generates only one tight focus (which means that the size satisfies the requirement in UNCOVER). So, we can use the similarity of the UNCOVER scanned images to identify if the constraint is satisfied or not. Other metric can be use as well: One can use ToF method to measure the distance that the returned photons travelled. If UNCOVER generates a single focus, there is only one strong peak showing up in the measurement. We expect many other detection methods may serve as the metric as well.

Proposition 2.1.1 shows 3D objects can be treated as 2D objects via projection, if the assumption in the proposition is satisfied. A natural question to ask is how strong these assumptions are. In other words, how small the axial extent should be in order to enable such projection. Here, we will give some numbers based on our second experiment (Fig. 5). In the second experiment, the side length of the full aperture is 0.6 mm and the distance from the wall to the object is $d = 0.55$ m. Each sub-aperture pair has a maximum side length $s' = \frac{0.6 \text{ mm}}{14} \times 2 = 86 \mu\text{m}$. Thus, the upper bound for the axial extent δz of the object is (Eq. S11)

$$\delta z \leq \min \left\{ 0.2d, \frac{2\lambda d^2}{5s'^2} \right\} = \min \left\{ 0.2 \times 0.55, \frac{2 \times 532 \times 10^{-9} \times 0.55^2}{5 \times (86 \times 10^{-6})^2} \right\} = \min\{0.11, 8.7\} = 0.11 \text{ m}. \quad (\text{S45})$$

Thus, the maximum axial extent is mainly dependent on the distance between the wall and the object.

If objects in the scene are distributed at significantly different distances, filtering methods need to be applied to UNCOVER. For instance, time-resolved measurement can be combined with UNCOVER to confine the axial range of the filtered signal. With this filtering, the effective axial extent of the object function can be confined in order to satisfy the condition in Proposition 2.1.1. Without filtering, UNCOVER may have degraded performance in generating a tight focus or even fail, depending on the specific settings. It's worthwhile to point out that the tight focus formed with filtering can be scanned over larger distances by superposing a defocus phase term over the phase solution. This range is not limited by the constraint on the axial extent (Eq. S11).

In UNCOVER, it is required that the focus size in optimizing phase offset among the pairs to be smaller than the hidden object. As the numerical aperture of the focus in such optimization depends on the size of the sub-apertures and the distance between the wall and the hidden target (Eq. S8), proper demagnifying system might be required. If there are multiple large objects (or a single large object), it might be tricky/impossible to de-magnify the sub-apertures such that they meet the constraints in UNCOVER. In this case, other techniques should be used to filter the returned signal. Follow the same logic in confining the axial extent of the effective object function, time gated/coherence gated measurement can be used to restrict the effective size of the objects such that the size is small and fulfills the constraints in UNCOVER. We also note that the scan range in UNCOVER is related to the memory effect range associated with the wall [6]. For object that is larger than this scan range, the field of view (FOV) needs to be increased in UNCOVER in order to image the entire object. This can be done by optimizing multiple foci at different positions. By stitching the FOVs associated with each individual focus, the overall FOV can be expanded, as stated in the Discussion part of our main manuscript.

We notice there is another paper uses segmented pupil to perform adaptive optics (AO) that looks similar to UNCOVER [7]. This AO method assumes that light from each segment of the pupil can form a focus (with unknown deflection and phase offset). This focus is raster scanned and the scanned image is compared with the reference image to now the deflection. In UNCOVER, however, we do not have such focus to begin with, an reference image is infeasible as well. The focus generated by one optimized sub-aperture is larger than the object. Thus, image of the hidden object cannot be formed by raster-scan of this focus. In optimizing the phase offset, the AO method use a single reference and no constraint is needed with respect to the distance between the two pupil segments in the optimization. In contrast, UNCOVER heavily relies on the confined size of the sub-aperture pair to generate a tight focus. Thus, UNCOVER is fundamentally different from the AO method.

It is believed that conventional wavefront shaping is unable to generate a focus on a large, homogeneous sample, as suggested by Katz et. al [8]. Here, we showed that with constraint on the aperture size in the optimization, a tight focus can be generated without exploring non-linear feedback. However, it should be

noted that if the sample is too large (say close to infinity in the extreme case), UNCOVER will not generate a tight focus as well. In this case, UNCOVER is not exempt from the discussion in [8].

3 PBR as a function of the initial signal

To investigate the peak-to-background ratio (PBR) that UNCOVER can achieve under different conditions, we conducted simulations by changing the initial number of photons received by the detector. In this simulation, the random phase shift (which characterizes the scattering of the wall) kept unchanged while the input light power was adapted to different levels. We also used the same target in this simulation. Apart from the signal reflected by the target, we added a background to the signal to imitate reflected photons from elsewhere, and Poisson noise was then simulated.

Figure S4 shows the simulation result. We iterated through the whole set of Hadamard basis for 3 times in this simulation.

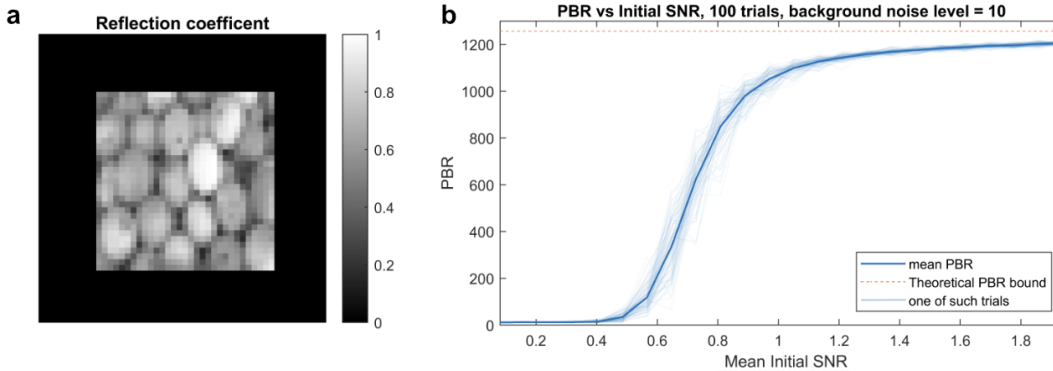


Figure S4: **a**, reflection coefficient of the target used in this simulation. **b**, peak-to-background ratio (PBR) as a function of the mean initial SNR (the SNR detected at the beginning of Step 2 in the optimization, averaged over all sub-apertures). In this simulation, in total $Q = 25$ sub-apertures were used, and $N^2 = 8^2 = 64$ independent modes were simulated in each sub-aperture. The color of the line in the legend representing result for one of such trials is emphasized for better illustration.

We expect the PBR grows gradually as the mean initial SNR approaches 1. As we plotted the final PBR against the mean initial SNR, SNR measured using some sub-apertures can be higher than the mean SNR. That is why we see an increase that appears earlier than mean SNR of 1. The PBR increases steeply as the mean initial signal level approaches the noise level (SNR approaches 1) and then plateaus as we further increase the mean initial signal. Supplementary Video 1 shows the foci of all sub-apertures and the final UNCOVER focus in one example trial.

4 Cumulative error in updating phase offset

As aperture synthesizing is crucial for generating a sharp focus, we investigated the error in finding the relative phase offset using pairs. We require the sub-apertures in the pair to be adjacent to ensure generation of a tight focus, thus, phase error in the reference will “propagate” to the sub-aperture being updated. This means that noises accumulate when the number of sub-apertures increases. As such, studying the noise as a function of the number of sub-apertures is useful for us to understand the limits of UNCOVER.

For a better illustration, we chose to update the phase offset in a more straightforward but less sophisticated way: we updated the offset along a “snake” trajectory rather than the “spiral” one that is used in our experiments.

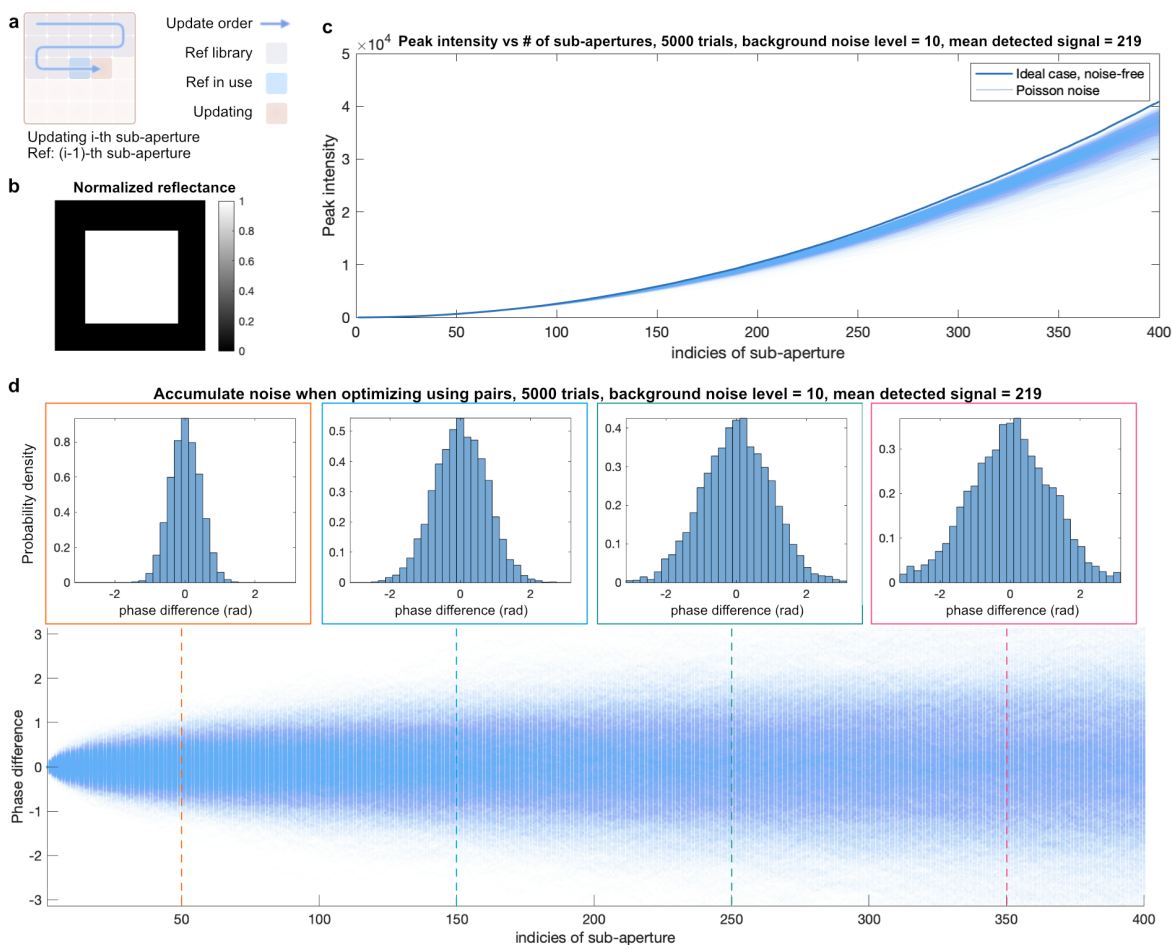


Figure S5: **a**, tuning the phase offset along the snake line. When sub-aperture i is being updated, the one which gets updated in step $i-1$ is chosen as the reference. Thus, the noise accumulates every time we update the phase offset. **b**, the normalized reflectance of the object used in this simulation. **c**, peak intensity as a function of the number of sub-apertures. The color of the line in the legend representing result for one of such trials (denoted by “Poisson noise”) is emphasized for better illustration. **d**, the phase error for each of the sub-aperture. The true phase offset is obtained in simulation when no noise is added. Figures inserted above are the histograms of the phase errors for the 50th, 150th, 250th, and 350th sub-apertures. “Mean detected signal” in **c** and **d** is the mean signal detected by opening one of the sub-apertures.

In this simulation, we set the mean signal detected by opening one of the sub-apertures equal to the mean value where the plateau begins in Fig. S4 (i.e. the mean signal value after optimization with mean initial SNR equals 1). To isolate the contribution of the noise in optimizing individual sub-apertures, we conducted the simulation in the following way:

In optimizing the phase mask for an individual sub-aperture, no noise is simulated. Poisson noise was

simulated in tuning the phase offset, and we ran 5000 trials to get the distribution of the phase error. We also simulated such tuning process in absence of the noise for obtaining a ground truth of the phase offset. Phase difference in Fig. S5d is the difference between the ground truth and the phase offset we obtained when Poisson noise is added.

The probability of the phase difference falls in range $[-\frac{\pi}{2}, \frac{\pi}{2}]$ is around 90% up to the 240th sub-aperture, as we found in our simulation. And the peak intensity when using all 400 sub-apertures is close to the ideal case for most of the trials, as Fig. S5c shows. If we want to keep such fidelity (Probability that is greater than 90%), the distance between any sub-aperture and the center sub-aperture should be less than 240 sub-apertures. Using the the spiral order we discussed in the paper, this distant limit indicates that we can use ~ 240 -by- 240 sub-apertures when considering the diagonal direction. Thus, the final focus can be shrunk by over 200 times compared with the one obtained by using one sub-aperture. With a higher SNR, this can be further increased.

5 UNCOVER focus quality as a function of sub-aperture size

We conclude, in section 2 of the Supplementary Note, that UNCOVER generates a sharp focus at C_m given the criterion is satisfied. Here, we want to investigate how the shape of the final focus changes when the criterion is broken.

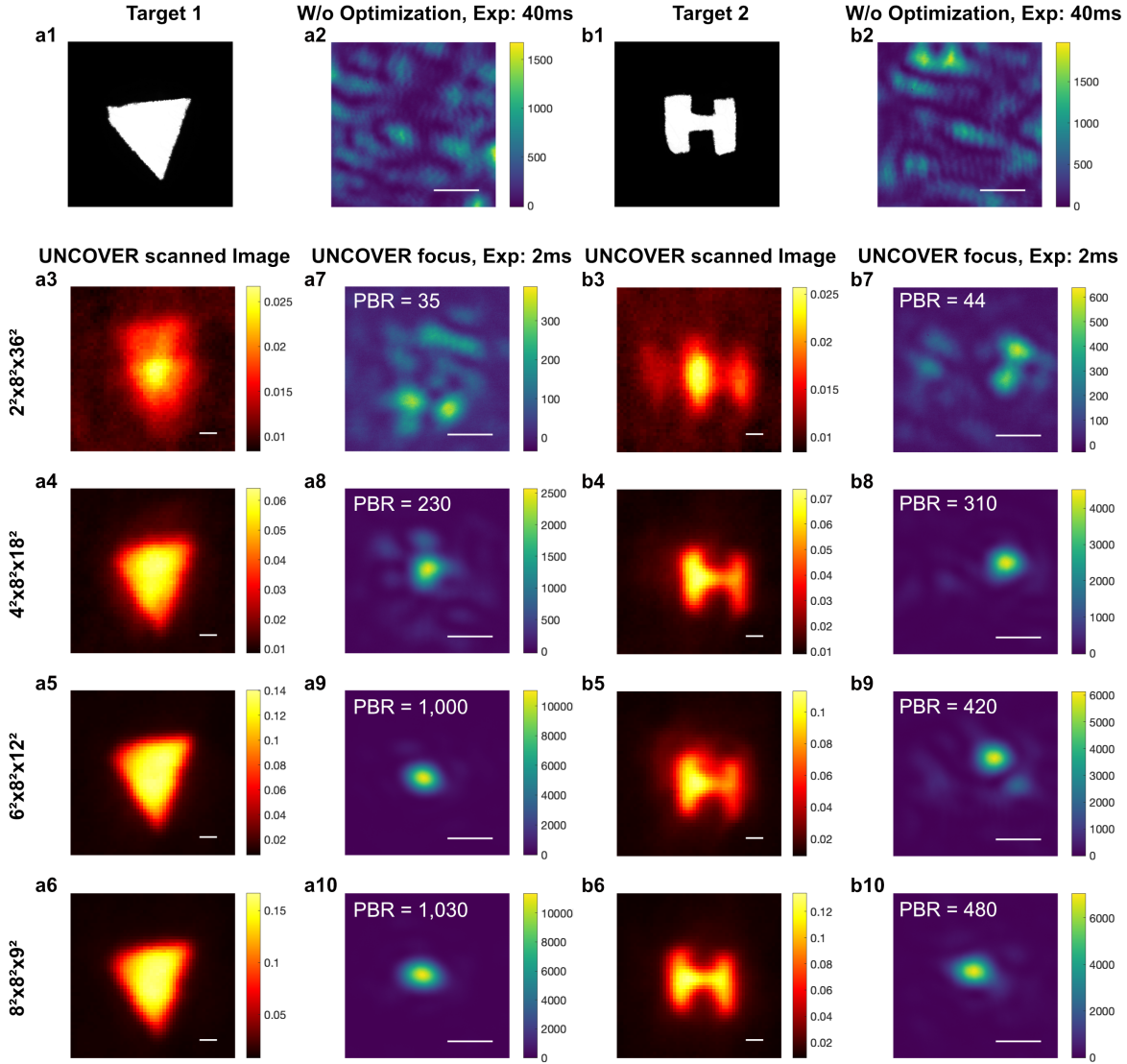


Figure S6: UNCOVER results when using different sub-aperture sizes. **a** and **b** are the results using target 1 and 2, respectively. The number on the far left of the figure denotes settings used for results in this row: $x^2 \times y^2 \times z^2$ means that there are x^2 sub-apertures, each sub-aperture has y^2 independent modes, and a square of z -by- z pixels on the SLM are treated as one independent mode. The side length for each sub-aperture is proportional to $y \times z$. For better illustration, we set different exposure time of the camera to capture UNCOVER foci (2 ms) and the speckle patterns without optimization (40 ms). A square of side length ≈ 0.35 mm is illuminated when using the full aperture. Length of the scale bars: 1 mm.

In this experiment, we set our parameters such that the full aperture generated by those parameters corresponded to the same area on the SLM. To be specific, the products of all the terms on the far left of Fig. S6 are the same, meaning that the ultimate numerical apertures for all the settings are the same. The last row of Fig. S6 shows the results we get when the constraint of UNCOVER is satisfied. Others show the results when the constraint is broken.

When the size of the sub-aperture is too large, the “focus” deviates from an ideal one. Discrepancies between the scanned image and the real target are easy to be noticed in Fig. S6 a3 and b3. As we decrease the size of sub-apertures, we gradually get a single focus, as shown in Figs. S6 a6 and S6 b6. Despite of this improvement, we noticed that the PBR improvement from Fig. S6 b9 to Fig. S6 b10 is minor. This is because less photons are used in optimizing one sub-aperture, resulting a decreased SNR.

It is worth noting that the shape of the object converges to the ground truth when we gradually decrease the size of the sub-aperture until it meets the requirement in UNCOVER. This also indicates that we can use it as a metric to tell whether UNCOVER generates a single focus when it is infeasible to obtain a rough gauge of the object size.

6 Imaging a hollow target

In the derivation in section 2 of the Supplementary Note, we proved that UNCOVER can generate a focus at the “center” of the target. Here, we conducted an experiment to investigate whether UNCOVER would produce a focus at the center of a hollow target, which consists of two squares as shown in Fig. S7a.

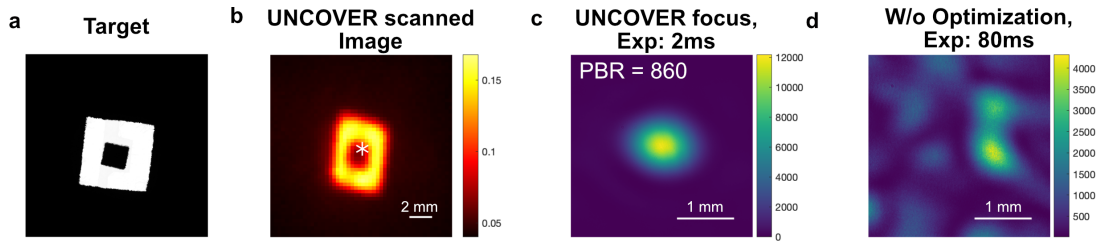


Figure S7: UNCOVER result of imaging a hollow object. In this experiment, $Q = 196$ sub-apertures (14×14) were used. A square of side length ≈ 0.61 mm is illuminated when using the full aperture. **a**, image of the target. **b**, UNCOVER result. The focus was initially formed at the white asterisk *. **c**, image of the UNCOVER focus, and **d** the speckles without performing optimization.

As shown in Fig. S7b, the focus located at the inner black square rather than the bright area where the reflectivity is much higher. This verifies that UNCOVER is very different from the conventional feedback based wavefront shaping. The maximizing problem UNCOVER solves is equivalent to maximizing the intensity at the center of the object, where the reflection coefficient can be as low as zero, as shown in this experiment.

7 Resolution in UNCOVER

To quantify the resolution in UNCOVER, radial profiles were extracted. The radial profile was fitted by a single Gaussian distribution. Full width at half maximum (FWHM) of the fitted curves was measured. As shown in Fig. S8c, the mean resolution is measured to be 0.57 mm.

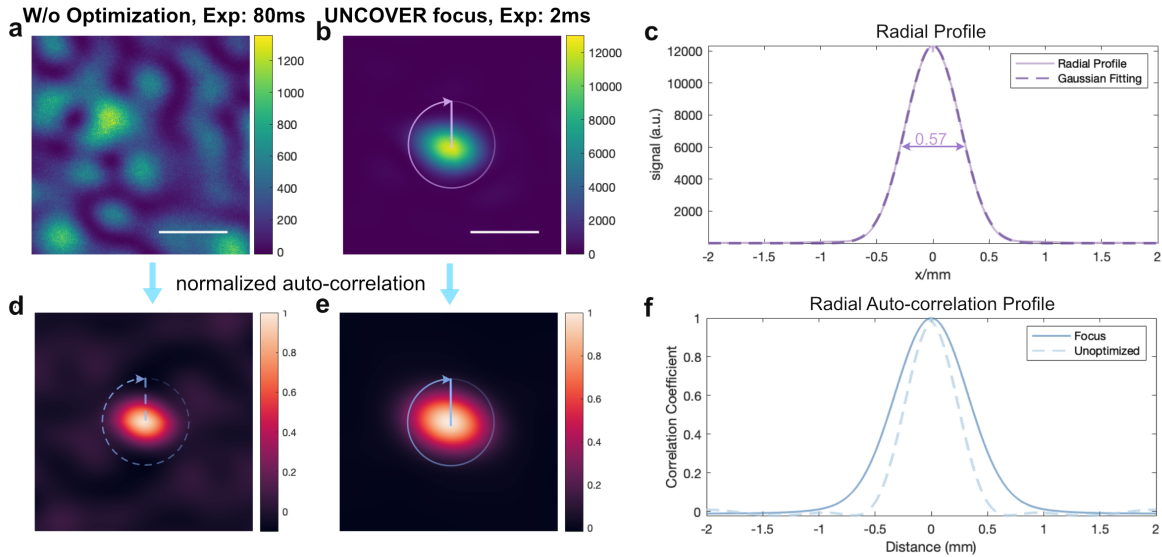


Figure S8: Resolution measurement of UNCOVER. This example uses the data from Fig. 5 of the main paper. **a**, speckle pattern captured before optimization. **b**, UNCOVER focus obtained after optimization. **c**, the radial profile that is obtained by averaging over a circle (one example circle is shown in **b**). Gaussian distribution is used to fit the curve. And the fitted curve is used to calculate the full width at half maximum (FWHM). **d** and **e** are the auto-correlation maps of **a** and **b**, respectively. **f**, the correlation radial profiles are averaged along the circles like those shown in **d** and **e**. Scale bar: 1 mm.

To compare the resolution of UNCOVER with the diffraction limit, auto-correlation of the unoptimized speckle pattern and the focus generated by UNCOVER were calculated. The correlation coefficient maps are shown in Fig. S8d and e. The FWHM of the correlation profile of UNCOVER is in general 1.5 times wider than that of the speckle pattern. Although UNCOVER doesn't achieve the ideal diffraction limit, it is close to the diffraction limit, which is a significant improvement over existing ToF methods.

8 Collection efficiency in UNCOVER and ToF methods

ToF methods need to confine the area of detection to encode the shape of the target into the time differences of the arriving photons. This confinement in return limits the distance that ToF methods can deal with. In contrast, UNCOVER considers only the power of the detected light. Thus, almost no restriction is needed in the area on the wall being detected in UNCOVER (except that light from the full aperture should be avoided). By imaging the detector onto the wall, we can derive that the number of photons being detected in UNCOVER is asymptotically independent of the distance between the wall and the detector. In contrast, in ToF methods, the aforementioned confinement leads to an inverse-square type drop-off in the number of photons it can detect with respect to the distance between the wall and the detector.

Here, we calculate the number of photons being detected in UNCOVER and ToF method while assuming the laser power, detector sensitivity, active area of the detector, the collecting lens, and the distances are the same in both cases.

As the distance from the wall to the the detection unit D is in general far larger than the focal length f of the lens in use, we will assume that $D \gg f$ in the following derivation. Considering the fact that the radius of the lens r is also small compared with D , we also assume $D \gg r$. When the target is far away from the wall, the photons that are scattered off by the target are approximately uniformly distributed across all points on the wall. In the following discussion, we will assume this spatial invariant intensity to be I_0 . Refer to Fig. S9 for the definition of the different distances/lengths used in the following derivation.

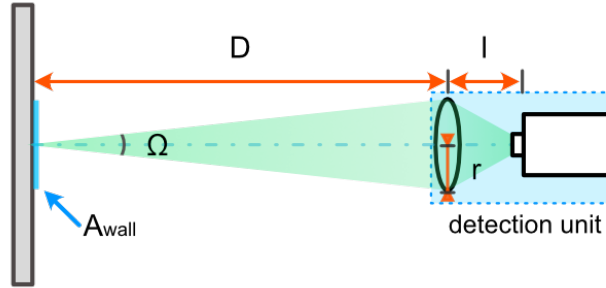


Figure S9: Detection scheme. Ω is the acceptance angle of the collection lens (here Ω is a solid angle). We assume an area of A_{wall} is detected. The distance from the lens to the wall is D , the distance from the lens to the image sensor is l and the radius of the lens is r . The focal length of the lens is f . The angles shown in the figure are for illustration and are different from the angles in our experiments.

In ToF method, an area of $1\text{mm} \times 1\text{mm}$ ($A_{\text{wall}} = 1 \times 10^{-6} \text{ m}^2$) is typically detected. Let the portion of light being detected by the detector with respect to the total power shine on an unit area on the wall be P . We know that P depends on the solid angle Ω as well as the location of the unit area. As we assume that the intensity is spatially invariant, we will ignore the dependence on the location. Thus, P is a function of Ω , which will be written as $P(\Omega)$. Using Taylor expansion at $\Omega = 0$, we have:

$$P(\Omega) = a_1\Omega + a_2\Omega^2 + \dots + a_n\Omega^n + \dots, \quad (\text{S46})$$

where $a_n (n = 1, 2, 3, \dots)$ are constant. The constant term is dropped as the ratio is zero when $\Omega = 0$. If Ω is small, we can keep the leading term and drop $O(\Omega^2)$, which gives:

$$P(\Omega) \approx a_1\Omega, \text{ given } \Omega \ll 1; \quad (\text{S47})$$

For $r \ll D$, we have the following approximation:

$$\Omega \approx \frac{\pi r^2}{D^2} \ll 1. \quad (\text{S48})$$

Thus, $P(\Omega)$ can be approximated as

$$P(\Omega) \approx a_1\Omega \approx a_1 \frac{\pi r^2}{D^2}. \quad (\text{S49})$$

Using this approximation, the number of photons being detected per unit time in ToF methods N_{ToF} is:

$$N_{\text{ToF}} = \frac{I_0 A_{\text{wall}} P(\Omega)}{h\nu} \approx \frac{I_0 A_{\text{wall}} a_1 \frac{\pi r^2}{D^2}}{h\nu} = \frac{a_1 \pi I_0 A_{\text{wall}} r^2}{h\nu D^2}, \quad (\text{S50})$$

where h is the plank constant, A_{wall} the area being detected on the wall, and ν the frequency of the light.

In UNCOVER, we do not need to confine the area of detection (except the apertures should be excluded), so the area being detected is mainly dependent on the active area of the detector. Assume the area of the detector is A_{Det} , and we image the wall onto the detector. Let's first calculate l , the distance between the lens and the image plane:

$$\frac{1}{f} = \frac{1}{D} + \frac{1}{l} \Rightarrow l = \frac{fd}{f+D} \approx \frac{fd}{D} = f. \quad (\text{S51})$$

Thus, the magnification power M is give by:

$$M = \frac{D}{l} \approx \frac{D}{f}. \quad (\text{S52})$$

So, in UNCOVER, the area being detected on the wall is

$$A'_{\text{wall}} = M^2 A_{\text{Det}} = \frac{D^2}{f^2} A_{\text{Det}}. \quad (\text{S53})$$

Thus, we can find the number of photons being detected per unit time in UNCOVER N_{UNCOVER} is

$$N_{\text{UNCOVER}} = \frac{I'_0 A'_{\text{wall}} P(\Omega)}{h\nu} \approx \frac{I'_0 \frac{D^2}{f^2} A_{\text{Det}} a_1 \frac{\pi r^2}{D^2}}{h\nu} = \frac{a_1 \pi I'_0 A_{\text{Det}} r^2}{h\nu f^2}. \quad (\text{S54})$$

An important finding is that N_{ToF} is inversely proportional to D^2 while N_{UNCOVER} is independent of D . This implies that the signal that UNCOVER detected is asymptotically independent of the distance between the detector and the wall. In contrast, signal in ToF system drops as the distance increases. It is worthwhile to point out that one cannot move the detector close to the wall in many practical NLOS settings. Thus, studying the enhancement in the number of photons that can be detected in UNCOVER compared with ToF type methods is important to find the operation range improvement of UNCOVER. The ratio of number of photons being detected in UNCOVER over ToF is given by

$$\frac{N_{\text{UNCOVER}}}{N_{\text{ToF}}} = \frac{a_1 \pi I'_0 A_{\text{Det}} r^2}{h\nu f^2} \frac{h\nu D^2}{a_1 \pi I_0 A_{\text{wall}} r^2} = \frac{I'_0 A_{\text{Det}} D^2}{I_0 A_{\text{wall}} f^2}. \quad (\text{S55})$$

To compare the number of photons being detected in UNCOVER and ToF method, we did an experiment to verify the signal decay. The results are shown in Fig. S10. In the experiment, a collecting lens of focal length $f = 32\text{mm}$ was used. We measured the signal starting at a distance of 0.5 away from the wall and increased the distance gradually. Each data point is the mean of 200 measurements and the length of error bar means their standard deviation. To match up with our experiment condition, the intensity for UNCOVER is decreased by 157 times ($\sim 50\pi$) as we use around 100 sub-apertures for most of our experiment. The detector used in our experiment has an active area of $3.7 \text{ mm} \times 13.0 \text{ mm}$ and the area being detected in ToF is a square with side length of 1 mm.

Using Eq. S55, we can find that the ratio of signal in UNCOVER over the signal in ToF method at a distance of 0.5 m is

$$\frac{N_{\text{UNCOVER}}}{N_{\text{ToF}}} = \frac{I'_0 A_{\text{Det}} D^2}{I_0 A_{\text{wall}} f^2} = \frac{1}{157} \frac{3.7 \times 13}{1 \times 1} \frac{0.5^2}{0.032^2} \approx 75. \quad (\text{S56})$$

In the actual experiment, we find that the ratio is approximately 87, which is slightly higher than the value based on our calculation. This is mainly due the fact that the scatted photon returning to the wall is not evenly distributed. In UNCOVER, a much larger area is being detected, which covers areas with higher intensities. As shown in Fig. S10, signal in ToF decreases much faster than UNCOVER. This shows that UNCOVER may potentially provide a larger operation range than the existing ToF methods. We note that

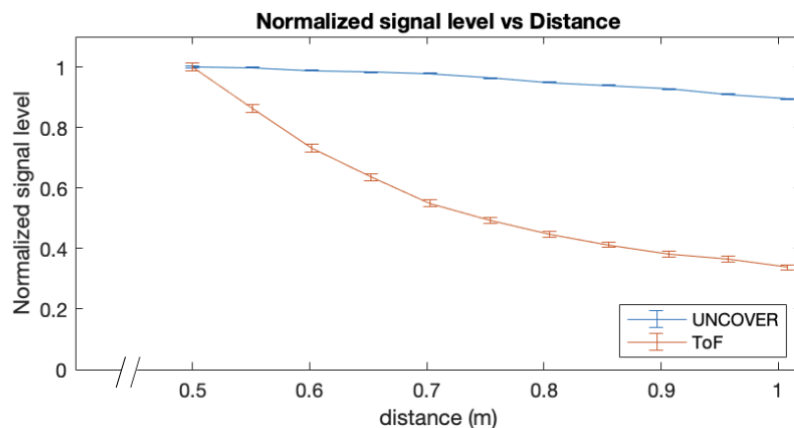


Figure S10: Power drop-off in UNCOVER and ToF method. The signals are normalized using their maximum value, respectively. Each point shows the mean of 200 measurements and the error bar shows the standard deviation of the 200 measurements.

the signals in UNCOVER exhibit a gentle decrease when the distance from the wall to the detector increases. This might also be caused by the uneven distribution of the scattered light, which violates the assumption that the intensity is spatially invariant.

In addition to the direct improvement in the detection efficiency, we want to point out that conducting feedback based wavefront shaping directly (without using pairs) also benefits in UNCOVER. Although applying feedback based wavefront shaping directly without using pairs is not guaranteed to, and probably will not, provide a focus, it delivers more light onto the target. With this pre-optimization, operation range of UNCOVER can be further increased.

References

1. Conkey, D. B., Caravaca-Aguirre, A. M. & Piestun, R. High-speed scattering medium characterization with application to focusing light through turbid media. *Optics Express* **20**, 1733–1740. ISSN: 1094-4087. <https://www.osapublishing.org/oe/abstract.cfm?uri=oe-20-2-1733> (2012).
2. Vellekoop, I. M. Feedback-based wavefront shaping. *Optics Express* **23**, 12189–12206. ISSN: 1094-4087. <https://www.osapublishing.org/oe/abstract.cfm?uri=oe-23-9-12189> (2015).
3. Horstmeyer, R., Ruan, H. & Yang, C. Guidestar-assisted wavefront-shaping methods for focusing light into biological tissue. *Nature Photonics* **9**, 563–571. ISSN: 1749-4893. <https://www.nature.com/articles/nphoton.2015.140> (2015).
4. Popoff, S. M., Lerosey, G., Fink, M., Boccarda, A. C. & Gigan, S. Controlling light through optical disordered media: transmission matrix approach. *New Journal of Physics* **13**, 123021. ISSN: 1367-2630. <https://doi.org/10.1088%2F1367-2630%2F13%2F12%2F123021> (2011).
5. Jang, J. *et al.* Complex wavefront shaping for optimal depth-selective focusing in optical coherence tomography. *Optics Express* **21**, 2890–2902. ISSN: 1094-4087. <https://www.osapublishing.org/oe/abstract.cfm?uri=oe-21-3-2890> (2013).
6. Freund, I., Rosenbluh, M. & Feng, S. Memory Effects in Propagation of Optical Waves through Disordered Media. *Physical Review Letters* **61**, 2328–2331. <https://link.aps.org/doi/10.1103/PhysRevLett.61.2328> (1988).
7. Ji, N., Milkie, D. E. & Betzig, E. Adaptive optics via pupil segmentation for high-resolution imaging in biological tissues. *Nature Methods* **7**, 141–147. ISSN: 1548-7105. <https://www.nature.com/articles/nmeth.1411> (2010).
8. Katz, O., Small, E., Guan, Y. & Silberberg, Y. Noninvasive nonlinear focusing and imaging through strongly scattering turbid layers. *Optica* **1**, 170–174. ISSN: 2334-2536. <https://www.osapublishing.org/optica/abstract.cfm?uri=optica-1-3-170> (2014).